

Paper

Int'l J. of Aeronautical & Space Sci. 16(3), 325–338 (2015)
DOI: <http://dx.doi.org/10.5139/IJASS.2015.16.3.325>

Wake Characteristics of Vane-Type Vortex Generators in a Flat Plate Laminar Boundary Layer

HoJoon Shim*

Korea Advanced Institute of Science and Technology, Daejeon 34141, Korea

Young-Hee Jo and Kyoungsik Chang*****

Hanseo University, Taeangun 32158, Korea

Ki-Jung Kwon****

Korea Aerospace Research Institute, Daejeon 34133, Korea

Seung-O Park*****

Korea Advanced Institute of Science and Technology, Daejeon 34141, Korea

Abstract

Experimental and numerical investigations were conducted to identify the wake characteristics downstream of two vane-type vortex generators over laminar flat plate boundary layer. Experimental study was carried out by using the stereoscopic particle image velocimetry. To describe the flow field around the vortex generator in detail, numerical study was performed. We considered two different planform shapes of vortex generator: triangular and rectangular shape. The height of the generator was chosen to be about the boundary layer thickness at the position of its installation. Two different lengths of the generator were chosen: two and five times the height. Wake measurements were carried out at three angles of attack for each configuration. Wake characteristics for each case such as overall vortical structure, vorticity distribution, and location of vortex center with downstream distance were obtained from the PIV data. Wake characteristics, as expected, were found to vary strongly with the geometry and angle of attack so that no general tendency could be deduced. Causes of this irregular tendency were explained by using the results of the numerical simulation.

Key words: Vortex Generator, Wake Characteristics, Laminar Boundary Layer, Stereoscopic-PIV

1. Introduction

As is well known, vortex generator is a typical passive flow control device and is used to delay flow separation in many engineering applications because of its geometrical simplicity and high performance as reviewed in Lin [1]. A study about vortex generator was first carried out by Taylor [2]. He found that streamwise vortices generated by the small vane vortex generators increase the near-wall momentum through momentum transfer from outer flow to near wall region. He

applied the vane-type vortex generators having the height of the order of the boundary layer thickness. Many experimental studies on aerodynamic flows with vortex generators were carried out since Taylor.

The height of the vortex generator is an important design parameter. The vortex generator whose height (h) is around boundary layer thickness is referred to as conventional vortex generator [1-4]. The vortex generator whose height (h) is shorter than local boundary layer thickness (δ) is referred to as low-profile vortex generator or micro vortex generator [4-

This is an Open Access article distributed under the terms of the Creative Commons Attribution Non-Commercial License (<http://creativecommons.org/licenses/by-nc/3.0/>) which permits unrestricted non-commercial use, distribution, and reproduction in any medium, provided the original work is properly cited.

© * Ph. D Student / currently Post Doc. Researcher
** Master Student
*** Assistant Professor
**** Principal Researcher
***** Professor, Corresponding author: sopark@kaist.ac.kr

7]. It was shown that the low-profile vortex generator could also be effective in spite of its shorter height for flow control [1].

The shape of the vortex generator is obviously an important factor as well. There are various vortex generator shapes; triangular, trapezoidal, rectangular, wishbone and doublet, etc. Torii and Yanagihara investigated the influence of a triangular vortex generator on heat transfer in laminar boundary layer [8]. Yanagihara and Torii also investigated the influence of vortex generator shape (triangular and rectangular) on heat transfer in laminar boundary layer [9]. They found that the rectangular vortex generator with higher angle of attack or larger frontal area showed the best heat transfer performance. Ashill et al. carried out experiments on wedge and triangular vane types of vortex generators of $h/\delta = 0.3$ on a bump [5]. Yao et al. measured flow field downstream of a single rectangular vortex generator using stereoscopic particle image velocimetry (Stereo-PIV herein after) [4]. Angele and Muhammad-Klingmann performed experiments over a separating boundary layer using rectangular vortex generator with three different heights and streamwise positions [10]. Lin et al. conducted experimental study to evaluate boundary layer separation control using triangular and trapezoidal shapes of small surface-mounted vortex generators on a high lift airfoil with a leading edge slat and a flap [11]. Studies on wishbone and doublet vortex generator were also conducted [12]. Godard and Stanislas carried out parametric study (angle of attack, length, transverse distance, etc.) of vortex generators (triangular and rectangular) and tested both co-rotating and counter-rotating configurations [13]. They found that triangular vortex generators produced a significant drag improvement compared to rectangular vortex generators. Velte et al. measured a flow field downstream of a row of triangular vortex generators mounted on a bump [14]. Significant reduction of reversed flow in separated region of the bump was observed when counter-rotating vortices were generated. Stillfried et al. carried out computations of flow on a bump with various rectangular vortex generator arrays in adverse pressure gradient boundary layer flow [15]. They found that vortex generators should be placed some distance upstream of the separation bubble location.

The representative shapes of the vane-type vortex generator were triangular and rectangular. Most of experimental and computational studies were mainly conducted in turbulent boundary layer. Kerho et al. conducted experimental study to examine the effect of wishbone and ramped cone generators on airfoil at low Reynolds number condition [16]. They found that the wishbone vortex generators and ramped cones delayed the onset of the separation bubble. Velte et

al. carried out the wake measurements in a wind tunnel and the flow visualization in a water tunnel past the rectangular vortex generator in laminar boundary layer [17]. They found that the vortical structure in the wake downstream of the vortex generator was much more complicated than a simple tip vortex structure. Yanagihara and Torii showed that the longitudinal vortices around the triangular vortex generator were composed of the main vortex, the corner vortices, and the induced secondary vortex [18]. In the laminar boundary layer, Velte et al. [17] and Yanagihara and Torii [18] showed that various vortices were generated by a vortex generator.

Previous studies mainly focused on aerodynamic control efficiency such as drag reduction, separation delay and vortical structure by a single vortex generator. Studies on the wake characteristics concerning development, interaction, and decay of various streamwise vortices depending on the generator shape at a same test condition seen be somewhat rare. In this regard, the present study was carried out. Wake characteristics of a triangular and a rectangular vortex generator were investigated. Stereo-PIV measurements in cross flow planes downstream of the two vane-type vortex generators were conducted. To gain a better understanding of flow physics associated with the multi-vortices within a laminar boundary layer, CFD simulations were also performed.

2. Experimental and Numerical Simulation

2.1 Test Facility and Test Conditions

Experiments were carried out in the subsonic wind tunnel of the Korea Aerospace Research Institute (KARI). The wind tunnel has a test section of 1.0 m width, 0.75 m height and 2.0 m length. Experiments were carried out at the wind speed of 10 m/s. The streamwise turbulence intensity was 0.06 %.

The flat plate on which vane-type vortex generator was installed was made of aluminum and was 990 mm wide, 1866 mm long, and 12 mm thick as sketched in Fig. 1 where the coordinate system adopted in this study is also shown. The flat plate was mounted at the center line of the wind tunnel test section. The leading edge of the flat plate was of a super-ellipse shape to prevent the leading edge separation [19]. The flat plate surface was covered with the black thin film to reflect the laser in one direction but not to allow the reflected laser into the camera [20]. Average surface roughness of the flat plate was below 0.05 μm .

Prior to the flow field measurement downstream of the vane-type vortex generator, the velocity profile on the flat plate was first measured by using 2-dimensional particle

image velocimetry (2D-PIV). The velocity profile at 750 mm from the leading edge was measured. Fig. 2 shows the comparison of the Blasius profile and the experimental data. The velocity profile was found to be that of the Blasius profile. The details of laminar boundary layer characteristics at the generator fixing point are summarized in Table 1.

2.2 Vortex Generator Configurations

In this study, we considered two different planform shapes of vortex generator: triangular and rectangular shape as shown in Fig. 3 where test conditions are also given. The height of the vortex generator was set to be the same as the boundary layer thickness at the installation location of 750 mm (see Fig. 1). The boundary layer thickness, δ , at the fixing point position was approximately 5 mm. Godard and Stanislas recommended that a minimum value of the

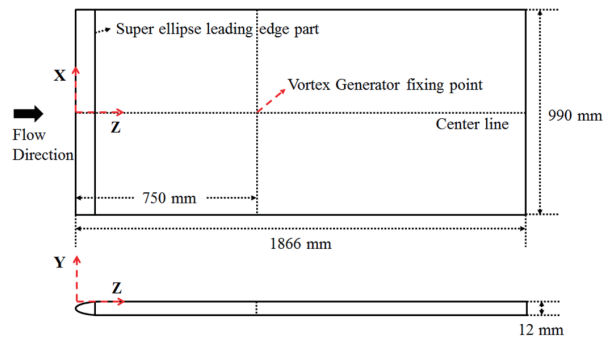


Fig. 1. Schematic of geometry and coordinate system of flat plate with super ellipse leading edge

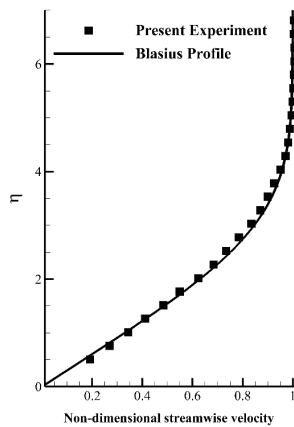


Fig. 2. Comparison of Blasius profile and experimental data

generator length should be two times the height [13]. Thus, we selected one length to be the two times the height. To look into the effect of length, we also chose a much longer length of five times the height. To investigate the influence of the angle of attack, three angles of attack (10°, 15°, and 20° angle of attack) were selected. To generate angle of attack, the vortex generator is rotated about the fixing point which is positioned at 2.5 mm ahead of the trailing edge.

2.3 Stereo-PIV Measurement

Stereo-PIV was used for the wake measurements. Fig. 4 is a schematic of the experimental setup. As briefly illustrated in Fig. 4, two high resolution CCD cameras whose angle with respect to the laser light sheet was 45 degrees were placed at both sides of the test section at the same distance from the laser light sheet. A 200mJ dual-head Nd:YAG laser of the QUANTEL Company was used. This provided the laser of 532nm wavelength. The laser was illuminated vertically in the x-y plane. As mentioned already, the surface of the flat plate was covered with black thin film not to allow the reflected laser into the CCD cameras.

PIV images were acquired using two high resolution (2048 x 2048 resolutions) cameras. As shown in Fig. 4, two CCD cameras were installed such that each could be moved freely for necessary alignment. Geared head of the Manfrotto Company was used for horizontality adjustment of the camera and lens. The camera tilt angle was adjusted by the scheimpflug [21]. To supply the tracer particles, Laskin nozzle using DEHS-oil was installed at the test section breather, far downstream of the vortex generator. The average diameter of the particles was about 1µm. The pulse generator of the BNC-555 model was used for synchronization between the laser and CCD cameras. Stereo-PIV time delay of 10µs between two images was decided by considering both the free stream

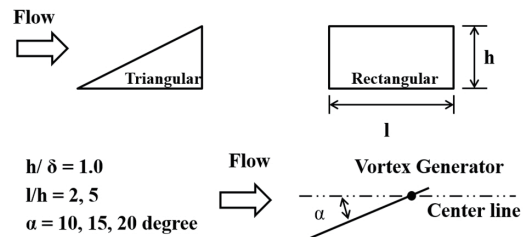


Fig. 3. Geometries of vortex generators and test conditions

Table1. Flat plate laminar boundary layer properties at the fixing point

| Parameter | Boundary layer thickness | Displacement thickness | Momentum thickness | Shape factor | Re_0 |
|-----------|--------------------------|------------------------|--------------------|--------------|--------|
| Laminar | 5 mm | 1.81 mm | 0.70 mm | 2.59 | 487 |

velocity and the field of view. By employing a system of mirrors, convex lens and cylindrical lens, the laser light sheet was generated over the flat plate. PIVview 3C program was used for image processing which was developed by PIVTEC GmbH and the German Aerospace Center's (DLR) PIV group [22].

Stereo-PIV measurements were performed at 7 downstream stations whose positions are listed in Table 2. In Table 2, Δz is the distance of the measurement station from the trailing edge of the vortex generator. Yao et al. showed that the vorticity contours exhibited a fairly concentrated vortex structure within $\Delta z/h \leq 20$ [4]. We thus selected these 7 stations within $\Delta z/h < 20$.

Prior to the wake measurement, calibration was performed at each measuring station. The magnification factor was 31 pixel/mm at all measuring stations. After calibration, one hundred image pairs were acquired at each measuring station and averaged for mean values.

The spatial resolution which affects the measurement result is defined by the interrogation window and overlap size. To estimate the effect of the spatial resolution, the image calculation was performed with respect to the various interrogation window and overlap size. First, the interrogation window size of 48×48 pixels was chosen through 2D displacement histogram analysis. Secondly, the overlap size was varied from 0% to 91%, and 75% overlap size was selected. Therefore, the 48×48 pixels and 75% overlap size implies that we have one vector for the area of $0.39 \text{ mm} \times 0.39 \text{ mm}$.

Uncertainty of the PIV measurement system comes from test instrument and image processing. The guideline of uncertainty analysis on PIV measurement is well described in the ITTC-Recommended Procedures and Guidelines [23]. Based on the ITTC Recommendation, uncertainty

analysis in the present study was carried out by following the AIAA standard [24]. Precision limits, P_u , P_v , and P_w were calculated based on the statistics of the measured u , v , and w . From 100 image pairs that were taken without a vortex generator, fluctuating velocities were statistically treated at the image center and the image corner. The precision limits were obtained to be $P_u = 0.03 \text{ m/s}$, $P_v = 0.02 \text{ m/s}$, and $P_w = 0.05 \text{ m/s}$ at the image center ($x = 0 \text{ mm}$, $y = 20 \text{ mm}$), and $P_u = 0.14 \text{ m/s}$, $P_v = 0.12 \text{ m/s}$, and $P_w = 0.14 \text{ m/s}$ at the image corner ($x = 20 \text{ mm}$, $y = 40 \text{ mm}$). Even though scheinpflug adapter was used to reduce out of focus at the image corner, velocity fluctuations due to blurred images increased the precision limits. We assumed that there was no bias error at the image center, and bias limits at the image corner were found to be $B_u = 0.003 \text{ m/s}$, $B_v = 0.006 \text{ m/s}$, and $B_w = 0.05 \text{ m/s}$. It can be said that the systematic or bias uncertainties are relatively small compared with the fluctuating or precision uncertainties. The final expanded uncertainties of the streamwise velocities were assessed to be $U_w = 0.1 \text{ m/s}$ at the image center and $U_w = 0.3 \text{ m/s}$ at the image corner.

2.4 Numerical Method and Computational Setup

The commercial CFD program [25] has been used to solve incompressible Navier Stokes equations. The second order discretization scheme in space and time was adopted and the correction of pressure-velocity was done using SIMPLEC algorithm. Time step was set to $\Delta t U_\infty/h = 0.0005$ and total simulated time steps were $2,000 t U_\infty/h$. Since the flow in the present work is started as the laminar boundary layer and then is developed toward the turbulent flow, where the Reynolds number based on the distance from the leading edge corresponds to about 5.0×10^5 , the transitional effect should be considered in the CFD simulation. For transitional

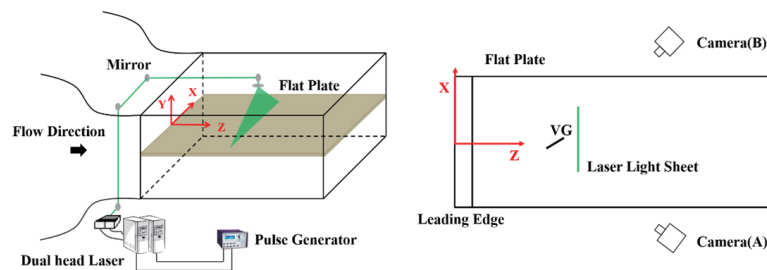


Fig. 4. Experimental setup, coordinate system and schematic of measurement system

Table 2. Measuring stations

| Station No. | 1 | 2 | 3 | 4 | 5 | 6 | 7 |
|--------------|-----|-----|-----|-----|------|------|------|
| $\Delta z/h$ | 1.5 | 3.5 | 5.5 | 7.5 | 11.5 | 15.5 | 19.5 |

model, γ transition model based on $k-\omega$ SST model was employed [26].

The computational domain and boundary conditions are shown in Fig. 5. We comment here that the vertical and spanwise lengths of the computational domain were reduced to half of those of the experimental domain. The inlet conditions for the numerical simulation were set to be the same with experimental conditions; the uniform flow with the velocity of 10 m/s and 0.06% streamwise turbulent intensity. The commercial software ICEM-CFD of ANSYS was used to generate the grid system with a hexahedron structured cell. Basically H-type grid was adopted in the whole domain and O-type one around the vortex generator to concentrate grid points near the walls and improve the grid quality. However, in the case of triangular vortex generator, the generation of y-block was required to build O-type grid around the vortex generator. Along the streamwise direction, 70, 70, and 105 grid points were assigned, respectively at upstream, the inside and downstream of the vortex generator. In spanwise direction, 106 grid points were put with dense distributions near the vortex generator. To resolve laminar (upstream of the vortex generator) and turbulent (downstream of the vortex generator) boundary layer correctly, the first grid points off the plate wall was put at $0.36 \times 10^{-3}h$ which corresponded to $y^+ < 1$ downstream of the vortex generator. We confirmed the simulated laminar boundary layer without the vortex generator case agreed well with the velocity profile of the 2D-PIV and the analytic Blasius solution. The number of total cells were 6.1×10^6 and 5.7×10^6 in the rectangular and the triangular vortex generator cases, respectively. The present CFD simulations have one vector for the area $0.07 \text{ mm} \times 0.09 \text{ mm}$ around the vortex generator.

3. Experimental Results

3.1 Mean Streamwise Flow

Figure 6 shows mean streamwise velocity contours at three downstream stations of the two vortex generators at 20° angle of attack. The velocity contours are those viewed toward the upstream direction (see Figs. 1 and 4). The

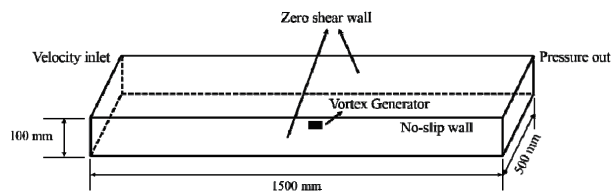


Fig. 5. Computational domain and boundary conditions

vortex generator projected onto each measurement station is also shown for convenience. We comment here that the height of the vortex generator was 5 mm. The formation of the streamwise vortex is clearly seen in Fig. 6. The pressure side of the vortex generator corresponds to the positive coordinate side of Fig. 6. Thus, the rotational direction of the streamwise vortex is counterclockwise as easily expected in these figures. Due to this vortex, the flow is swept upward in the pressure side region and downward in the suction side region resulting in greater streamwise mean velocity in the suction side. The mean flow structure shown in Fig. 6 is seen to be much more complicated than that in the results of Yao et al. [4]. Interesting result was the generation of an additional vortex at specific test conditions. A vortex generated around the tip of the vortex generator was referred to as primary vortex, and a vortex observed on the pressure side of the vortex generator as secondary vortex.

3.2 Streamwise Vorticity Distribution

Table 3 lists the streamwise peak vorticity of the primary vortex of the two shapes of vortex generator at $\Delta z/h = 1.5$. For the case of the triangular generator, the peak vorticity is seen to increase with angle of attack at both length conditions. However, we see that this tendency does not hold for the cases of rectangular generator. We observe from Table 3 that the peak vorticity of the rectangular generator increases with angle of attack when $l/h = 2$ but decreases with angle of attack when $l/h = 5$. This reverse trend of the peak vorticity of the rectangular generator when $l/h = 5$ will be discussed later.

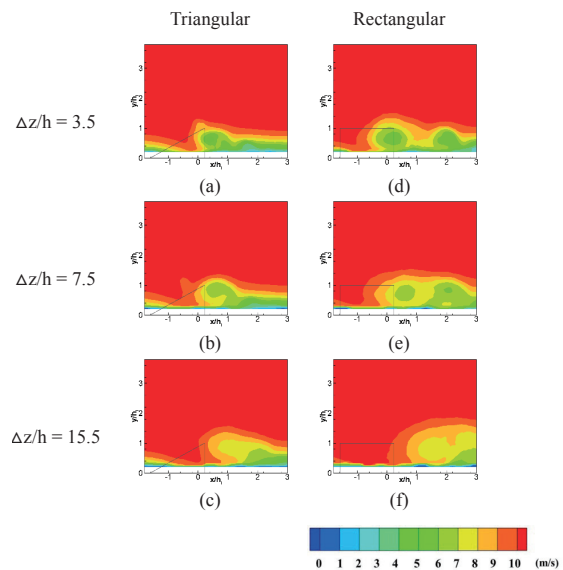


Fig. 6. Mean streamwise velocity contours of the experiment ($h/\delta = 1.0$, $l/h = 5$, and $\alpha = 20 \text{ deg.}$)

To examine the development properties of the streamwise vortex with downstream distance, variations of the peak vorticity with $\Delta z/h$ are depicted in Fig. 7. We recall here that Δz is the distance between the measuring station and the trailing edge of the vortex generator. The streamwise peak vorticities downstream of the generator were divided by the peak vorticity at $\Delta z/h = 1.5$. Thus, at $\Delta z/h = 1.5$, $\omega/\omega_{\max} = 1.0$. Fig. 7 shows the variation of the streamwise peak vorticity of the primary vortex for the two vortex generator shapes of two

different lengths at three angles of attack. Fig. 7 demonstrates evidently the effects of generator length and angle of attack. However, we can hardly deduce any general tendency. Fig. 7 (f) shows that the decay behavior of the triangular generator is much greater than that of the rectangular generator in the near wake region. From Fig. 7 (f) and Table 3, we see that even though the largest vorticity was generated by the triangular generator, the vorticity corresponding to the rectangular generator decayed much more slowly in this specific case.

Table 3. Peak vorticity of two shapes of vortex generator at $\Delta z/h = 1.5$

| Length | α (deg.) | Triangular (1/sec) | Rectangular (1/sec) |
|---------|-----------------|--------------------|---------------------|
| l/h = 2 | 10 ° | 3697.45 | 2786.00 |
| | 15 ° | 4565.06 | 4219.52 |
| | 20° | 5196.60 | 6722.17 |
| l/h = 5 | 10° | 4202.69 | 5226.77 |
| | 15° | 5474.86 | 4645.00 |
| | 20° | 7100.74 | 3924.52 |

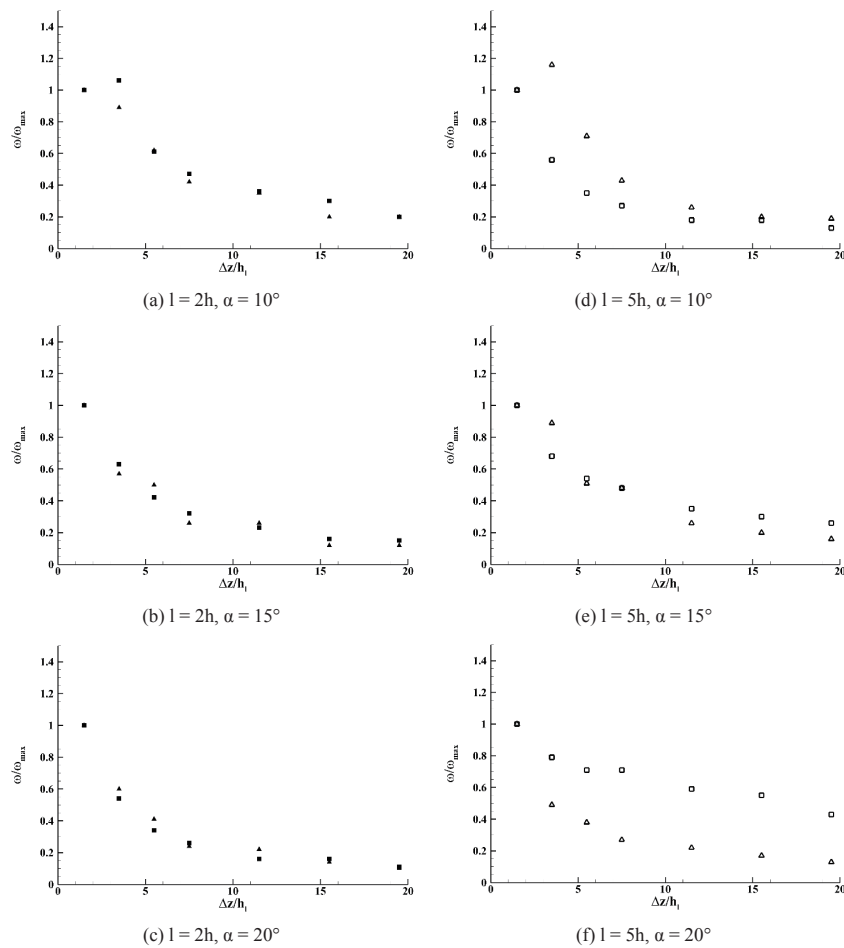


Fig. 7. Peak vorticity decay behavior of primary vortex of two shapes of vortex generator (Δ : triangular and \square : rectangular vortex generator)

3.3 Vortex path

Figure 8 shows the lateral and the vertical path of the vortex center for various cases. The center of the vortex was located by using the maximum vorticity method [4, 27, 28]. The lateral position is referenced to the trailing edge location when $\Delta x = 0$. Positive Δx in the figure denotes the distance in the pressure side direction. The vertical position of the streamwise vortex center is observed to be located in the region between $0.7h$ and $1.0h$ at all downstream stations for the case of the rectangular generator, and between $0.5h$ and $0.8h$ for the triangular generator. We see that the vortex of the triangular generator is generated at a considerably lower position than those of the rectangular cases. Compared with the lateral path variation, we see that the vertical paths do not vary much with downstream distance. We clearly see from

Fig. 8 that the vortex center moves away from the trailing edge position in the direction of pressure side (Δx direction) with downstream distance. This reflects a simple fact that the mean flow in the wake is deflected to the right, that is, to the pressure side. The lateral variation of the vortex center increases with angle of attack. From the figure, we find that the distance between the centerline and the lateral position is largest in the case of rectangular generator, and shortest in the triangular generator. We also see that the vortex center position differences among the two generator shapes for the case of $l/h = 5$ are greater than those for the case of $l/h = 2$.

3.4 Secondary vortex

An additional vortex is observed at downstream of the vortex generator in Fig. 6. The additional vortex is referred

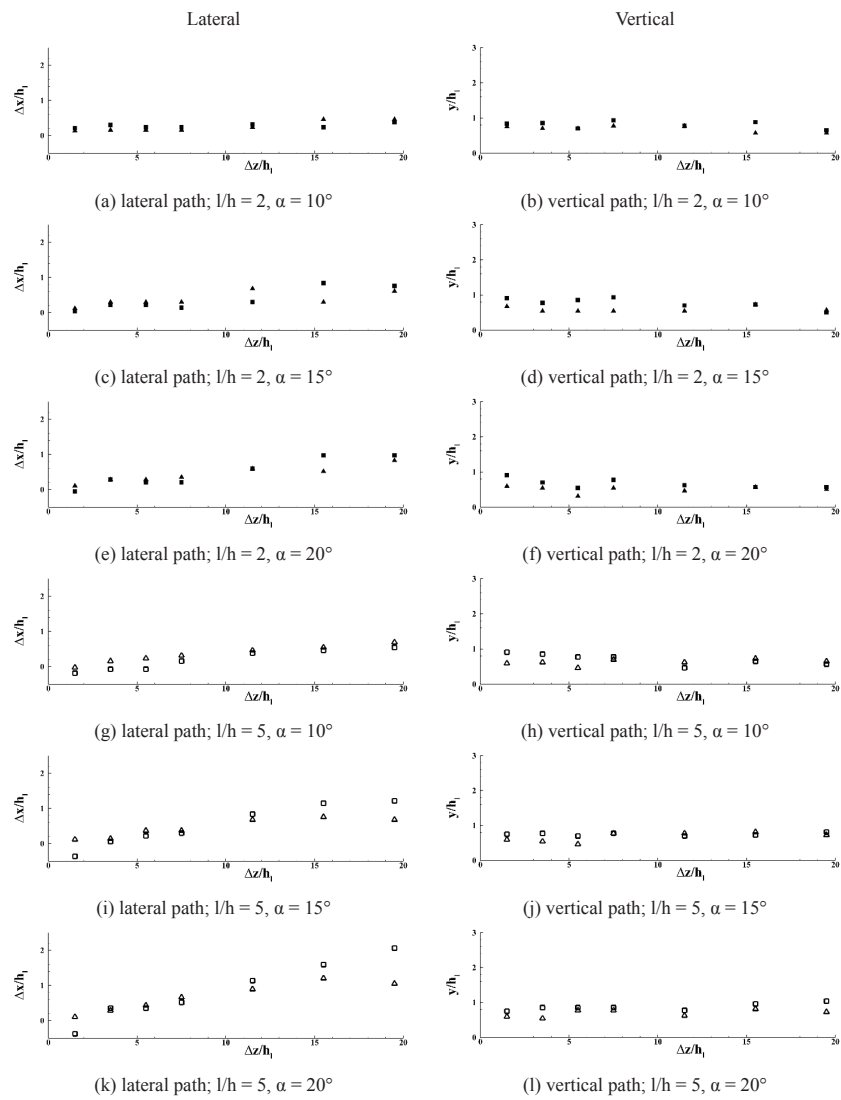


Fig. 8. The lateral and the vertical path of the primary vortex center (Δ : triangular and \square : rectangular vortex generator)

to as secondary vortex. Table 4 is a list of strength and center location of the primary and the secondary vortices at one specific case. The secondary vortices seen in Fig. 6 are related to a horseshoe-like vortex around the leading edge of the vortex generator [17]. The rotation direction of the horseshoe vortex on the pressure side is in the same sign with the primary vortex. According to Velte et al., various regimes of the multi-vortical structure exist [17]. The flow condition, the geometric parameters of the vortex generator, and the interaction between the primary vortex and the horseshoe vortices affect these various regimes of the multi-vortical structure. Velte et al. mentioned three different regimes, and the vortical structure of the present of Fig. 6 complies with the first regime of Velte et al. [17].

From Table 4, we see that the peak vorticity of the primary vortex of the triangular generator is larger than the rectangular case. In contrast to this, the peak vorticity of the secondary vortex is largest in the case of the rectangular generator, smaller in the triangular generator case implying that the horseshoe vortex around the rectangular generator is much stronger. It is interesting to note that, in the rectangular generator case, the peak vorticity of the primary vortex is less than that of the secondary vortex, which is rather unusual. In this respect, we examined the data at 15° angle of attack. At this angle of attack, we found that the peak vorticity of the primary vortex of the rectangular generator was 4645.0/s which was much greater than that of the secondary vortex which was 1960.93/s. We comment here that the secondary vortex was not observed when the angle of attack was 10° for the two vortex generators of $l/h = 5$. For the case of $l/h = 2$, the secondary vortex was observed only at 20° angle of attack for the two vortex generators. Moreover, the reverse trend of the peak vorticity of the primary and the secondary vortices at $l/h = 2$ and 20° angle of attack is not observed. As mentioned above, the peak vorticity of the primary vortex of the rectangular and the triangular generators in the case of $l/h = 2$ is increased as angle of attack increases; however, this peak vorticity increasing trend is not observed on the rectangular generator of $l/h = 5$. Thus, we confirm that the formation of the secondary vortex depends on the angle of attack and the length of the vortex generator. Detailed flow-field around the vortex generator will be discussed at CFD results.

The vertical positions of the secondary vortex of Table 4 are seen to be located slightly lower than those of the primary vortex. We also see that the primary and the secondary vortices of the triangular generator are generated at a considerably lower position than that of the rectangular case. From Table 4, we also found that the distance between the primary and the secondary vortices is larger in the case of rectangular generator, and shorter in the triangular case at this test condition.

3.5 Computational Results

As mentioned above, in the rectangular generator case, the peak vorticity of the primary vortex is less than that of the secondary vortex downstream of the generator when $l/h = 5$ and $\alpha = 20^\circ$, and this reverse phenomenon of the peak vorticity between the primary and the secondary vortex is not observed at 15° angle of attack of the rectangular generator and two angles of attack of the triangular generator. The peak vorticity of the primary vortex of the rectangular generator when $l/h = 5$ is decreased as angle of attack increases (see Table 3). To examine this phenomenon clearly, CFD simulations were performed for the case of $l/h = 5$. Fig. 9 shows the comparison of the streamwise velocity contours for validation of the CFD results. The CFD results of the locations and the structures of the primary and the secondary vortices are in reasonably good agreement with the experimental results.

Figure 10 shows that the various vortices are generated around the rectangular and triangular generators of $l/h = 5$ at 20° angle of attack. We comment here that the horseshoe vortex of the pressure side was referred to as the secondary vortex. From the CFD results, the peak vorticity of the primary vortex of the rectangular generator was 3260.6/s at $\Delta z/h = 1.5$ and the peak vorticity of the secondary vortex was 4467.2/s. In the case of the triangular generator, the peak vorticity of the primary vortex was 6025.3/s and that of the secondary vortex was 3221.1/s. This trend of the peak vorticity between the primary and the secondary vortex for both generators is in good agreement with the experimental results (see Table 4). Fig. 10. (a) shows that the horseshoe vortex of the suction side was merged with the primary vortex over the rectangular generator, and the vortical

Table 4. Variation of primary and secondary vortex ($l/h = 5$, $\alpha = 20^\circ$, and $\Delta z/h = 1.5$)

| | Primary vortex | | | Secondary vortex | | |
|-------------|----------------|--------------|-------|------------------|--------------|-------|
| | Peak vorticity | $\Delta x/h$ | y/h | Peak vorticity | $\Delta x/h$ | y/h |
| Triangular. | 7100.74 | 0.10 | 0.59 | 2072.49 | 1.30 | 0.27 |
| Rectangular | 3924.52 | -0.38 | 0.75 | 5185.72 | 1.38 | 0.51 |

structure of the primary vortex of the rectangular generator is weakened at $z = 760$ mm position ($\Delta z/h = 1.5$). In contrast with the rectangular generator, the horseshoe vortex on the suction side of the triangular generator is not generated in Fig. 10 (b). The vortical structure of the triangular generator at $z = 760$ mm ($\Delta z/h = 1.5$) is seen to be coherently retained when compared with the rectangular generator case. To

gain better understanding for the wake characteristics downstream of the vortex generator, the CFD simulations for both generators were carried out at angles of attack ranging from 5° to 30° at an increment of 5° .

Figure 11 shows the peak vorticity distributions of the primary vortex and the secondary vortex in the pressure side with six angles of attack at $\Delta z/h = 1.5$. In the case of the

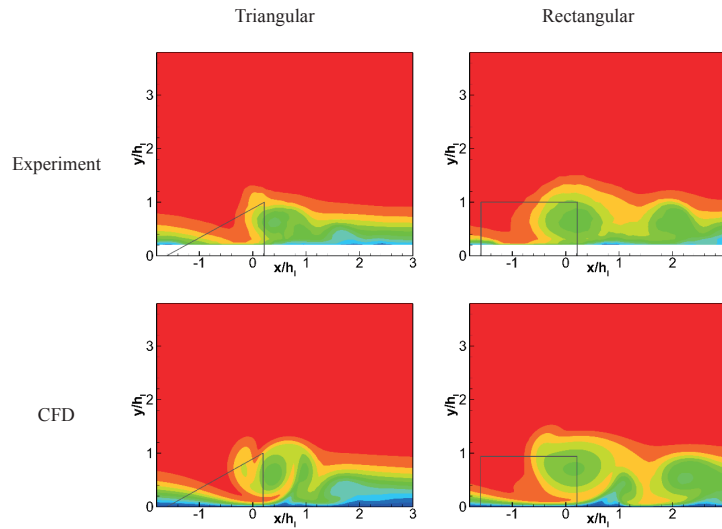


Fig. 9. Comparison of the streamwise velocity contours for validation of the CFD results

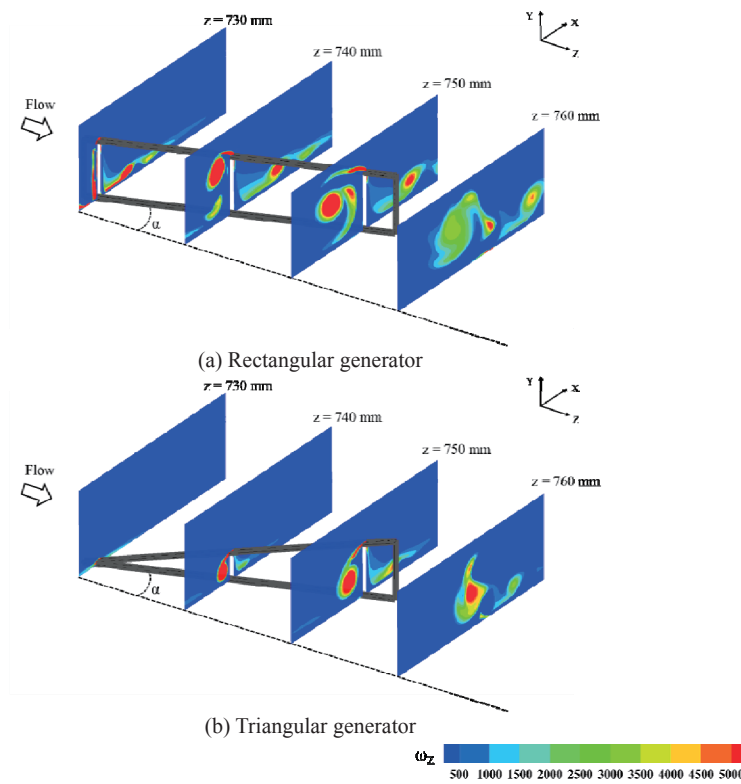


Fig. 10. Computational results of the rectangular and the triangular generators of $l/h = 5$ at 20° angle of attack

rectangular generator, maximum peak vorticity was found to occur at 10° angle of attack and the peak vorticity was decreased beyond 10° angle of attack. This decreasing trend of peak vorticity at three (10°, 15°, and 20°) angles of attack is in accordance with the experiment data (see Table 3). We also see that the peak vorticity of the secondary vortex was increased with angle of attack and then decreased at 30° angle of attack. In the case of the triangular generator, the peak vorticity of the primary vortex was slightly increased with angle of attack whereas and the peak vorticity of the secondary vortex was rapidly increased up to 30° angle of attack.

In the case of 10° angle of attack, the streamwise peak vorticity of CFD results on the rectangular generator was 7133.7/s which was greater than that of the experiment (see Table 3 and Fig. 11). The peak vorticity of CFD at 15° angle of attack was 4653.0/s which is in reasonably good agreement with the experimental data. At 20° angle of attack, the peak vorticity of CFD was 3260.6/s, and lower than that of the experiment. Yao et al. mentioned that the CFD tends to underpredict the magnitude of peak vorticity and accurately predicting the vorticity is one area that needs to be improved [4]. Görtz showed that the overall velocity field for the delta wing at high angle of attack condition was well predicted by CFD, however, the numerical simulation underestimated the maximum velocities in the core of the vortex [29]. Lam and Wei mentioned that the lower peak vorticity in the experiments was caused by much larger spatial resolution

of the PIV as compared to those in the fine computational grid; however, the experimental and the numerical results showed very similar trend of vorticity variation [30].

Although the CFD result and the experimental data show the discrepancy of the streamwise peak vorticity, the qualitative relations between the primary vortex and the secondary vortex of the CFD results were in good agreement with the wake vortical structures of the experimental data. Therefore, the decay behavior was calculated and compared with the experimental results to identify the characteristics of the wake behavior. As mentioned above, the decay behavior is nondimensionalized by the peak vorticity at $\Delta z/h = 1.5$.

Figure 12 shows the CFD results of the decay behavior (see Fig. 7, $\omega/\omega_{s,max}$) with those of experiments for the three angles of attack of the rectangular and the triangular vortex generators in the case of $l/h = 5$. We see from Fig. 12 that the CFD results of the decay behavior for the rectangular generator are in good agreement with the experimental data at three angles of attack. In the cases of 10° and 15° angle of attack of the triangular generator, the decay behavior of the CFD results also corresponds well with the experimental data. However, Fig. 12 (c) shows that the decay behavior of the CFD result and the experimental data are quite different each other.

Figure 13 shows the vorticity contours for the rectangular vortex generator of $l/h = 5$ with six angles of attack at the fixing point plane. We recall here that the fixing point is located at 750 mm from the flat plate leading edge, $y/h = 1.0$ is

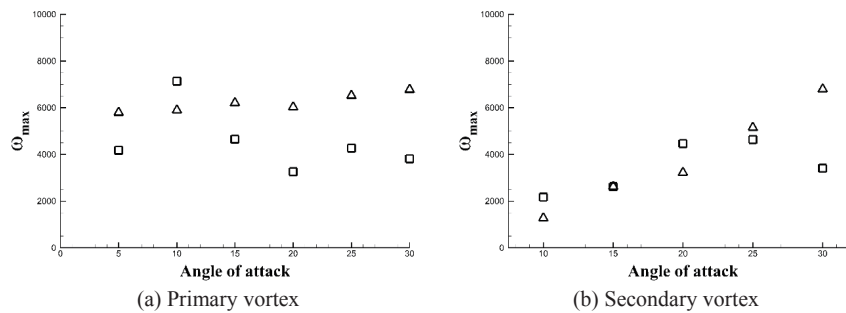


Fig. 11. Peak vorticity of the primary and the secondary vortex with six angles of attack at $\Delta z/h = 1.5$ (Δ : triangular and \square : rectangular vortex generator)

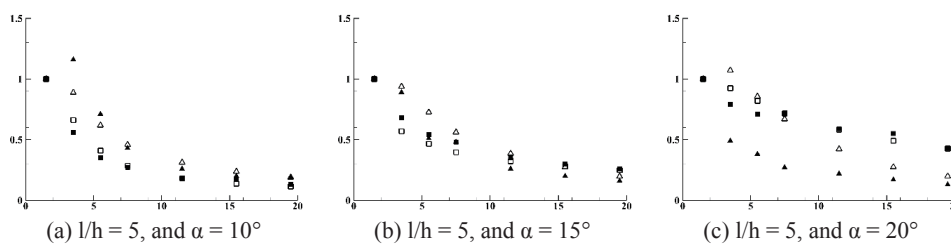


Fig. 12. Decay behavior of the primary vortex of the experimental and the computational results of the rectangular (\blacksquare : experiment, \square : computation) and the triangular (\blacktriangle : experiment, and \triangle : computation) vortex generators

the vortex generator tip, and $x/h = 0.0$ is the centerline of the flat plate. Positive x coordinate corresponds to the pressure side of the vortex generator. We see that the primary vortex is generated near the tip of the generator. The secondary vortex is observed at pressure of the generator. Velte et al. mentioned that a pressure distribution around the leading edge creates horseshoe-like vortices with two arms and a horseshoe-like vortex of the suction side is referred to as HS and the other one of the pressure side is referred to as HP [17]. The peak vorticity behavior of the secondary vortex shown in Fig. 11 (b) can be exposed again in Fig. 13. In Fig. 13 (f), the vortical structure of the secondary vortex is weaker than that of Fig. 13 (e). Fig. 13 also shows that the horseshoe vortex of the suction side becomes stronger as angle of attack increases, and the primary vortex is strongly influenced by the horseshoe vortex of the suction side beyond 10° angle of attack. Thus, the streamwise peak vorticity of the primary vortex beyond 10° angle of attack is decreased by the interaction between the primary vortex and the horseshoe vortex of the suction side. At 10° angle of attack condition, we see that the primary vortex was almost not influenced by the horseshoe vortex to result in the maximum peak vorticity of the primary vortex at this angle of attack at $\Delta z/h = 1.5$ (see

Fig. 11).

In contrast with the rectangular generator case, the peak vorticity of the primary vortex downstream of the triangular generator is higher than that of the secondary vortex when $l/h = 5$ and $\alpha = 20^\circ$ (see Table 4). Fig. 14 shows the vorticity contours of the triangular vortex generator at six angles of attack at the generator fixing point plane. Yanagihara and Torii showed that the longitudinal vortices around a single triangular vortex generator were consisted of main vortex, corner vortices, and induced vortex [18]. They mentioned that the corner vortices were formed in the corner between the generator pressure side and the plate, and the induced vortex was formed as a result of the redirectioning of the near-wall flow caused by the lower pressure behind the generator. The rotation direction of the induced vortex on the suction side is in the opposite sign with the primary vortex, and the induced vortex was only observed at downstream of the triangular generator.

In the present cases, we see that additional vortex over the suction side of the triangular generator was not observed. This explains the observation that the peak vorticity of the primary vortex increases slightly with angle of attack shown in Fig. 11 (a). From Fig. 14, we also see that the secondary

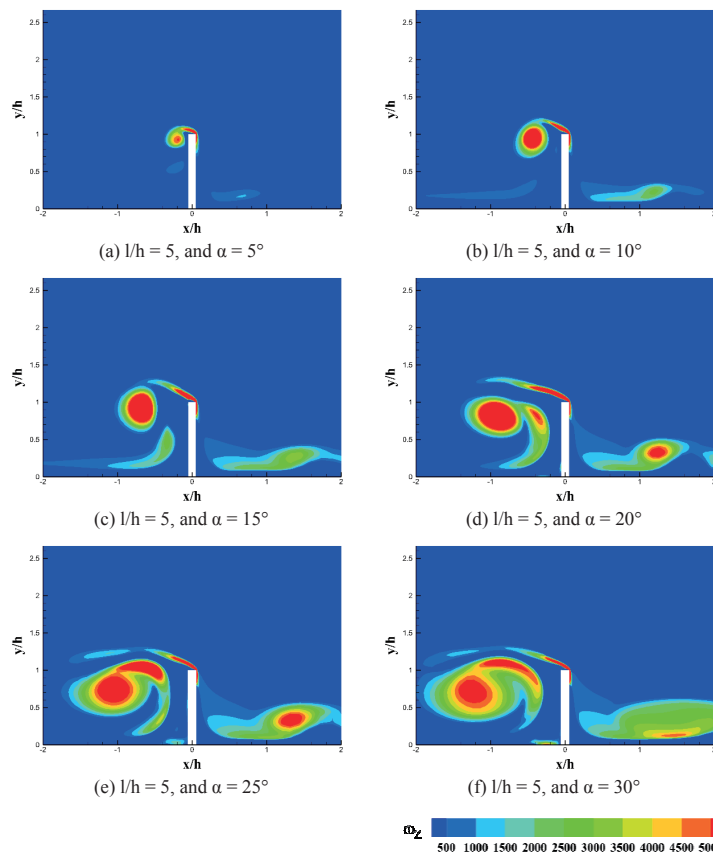


Fig. 13. Vorticity contours for the rectangular vortex generator of $l/h = 5$ at six angles of attack at the fixing point plane

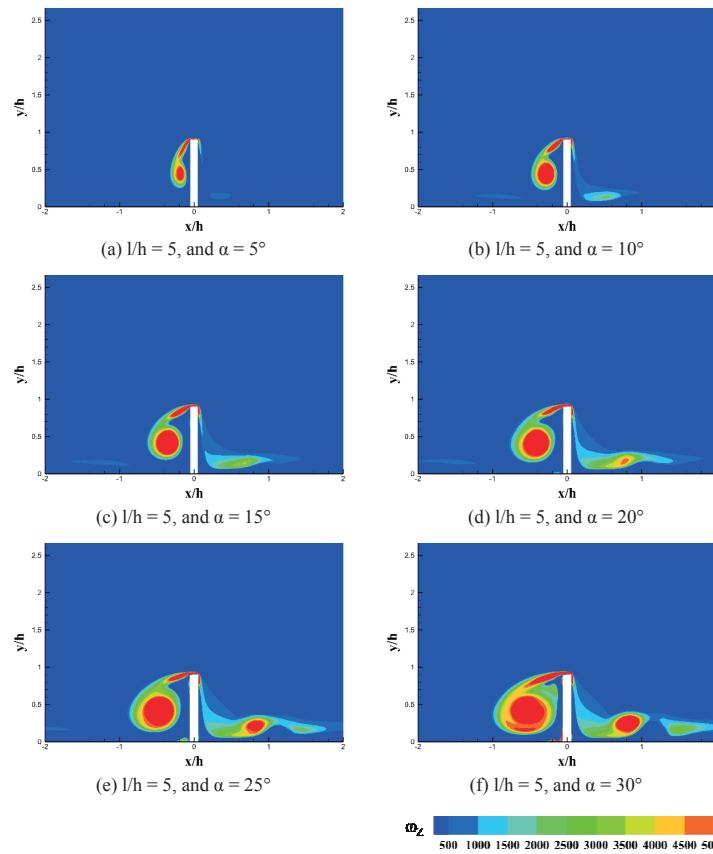


Fig. 14. Vorticity contours for the triangular vortex generator of $l/h = 5$ at six angles of attack at the fixing point plane

vortex on the pressure side gets stronger with angle of attack (see Fig. 11 (b)). Additional vortex on the pressure side was only observed at 25° and 30° angles of attack. The streamwise peak vorticity of the primary vortex was greater than that of the secondary vortex up to 25° angle of attack at $\Delta z/h = 1.5$. In the case of 30° angle of attack, the CFD simulations showed that the peak vorticity of the primary vortex was of the similar strength with that of the secondary vortex.

4. Conclusions

Experimental and numerical investigations were conducted to identify the wake characteristics downstream of two vane-type vortex generators over a flat plate laminar boundary layer. Experimental study was carried out by using stereoscopic particle image velocimetry. The triangular and the rectangular generators of two different lengths at three angles of attack were tested. The tendency of peak vorticity generation in the near wake region for each generator configuration was very sensitive to angle of attack and length of the generator. We observed two streamwise vortices at

downstream of the generator, the primary and secondary vortex, at some test cases illustrating that the flow structure is very complicated. The emergence of the secondary vortex depended on angle of attack and generator length. The decay behavior of the primary vortex was evidently influenced by the generator length and angle of attack. The vorticity decay characteristics at high angle of attack with downstream distance also depended strongly on the generator shape. This signifies that the initial peak vorticity strength in the near wake does not imply its strength tendency at further downstream stations. Trajectories of vortex core (or center) along downstream distance for each case were presented. It was found that the vortex of the triangular generator was formed at lower position than that of the rectangular generator. The lateral position of the vortex center of the triangular case was closer to the trailing edge than the rectangular generator case, all of them being located in the suction side in the near wake region.

For the cases of $l/h = 2$ and 5, the peak vorticity of the triangular generator was increased as angle of attack increased. The rectangular generator exhibited the increasing trend of the peak vorticity with three angles of attack at $l/h =$

2 case. However, for the case of $l/h = 5$, the peak vorticity of the rectangular generator was decreased as angle of attack increased. For the case of the rectangular generator of $l/h = 5$, the peak vorticity of the primary vortex was less than that of the secondary vortex at 20° angle of attack. CFD simulations showed that this phenomenon of the rectangular generator was caused by the interaction between the primary vortex and the horseshoe-like vortex of the suction side. CFD results of the triangular generator showed that the secondary vortex was not generated over the suction side of the generator, which explained why the peak vorticity of the primary vortex increased consistently with angle of attack.

Acknowledgement

This work was supported by Defense Acquisition Program Administration and Agency for Defense Development. (UC100031JD).

References

- [1] Lin, J. C., "Review of research on low-profile vortex generators to control boundary-layer separation", *Progress in Aerospace Sciences*, Vol. 38, Issues 4-5, 2002, pp. 389-420.
- [2] Taylor, H. D., "The elimination of diffuser separation by vortex generators", *United Aircraft Corporation Report No. R-4012-3*, 1947
- [3] Lin, J. C. and Howard, F. G., "Turbulent flow separation control through passive techniques", *AIAA 2nd Shear Flow Conference*, Tempe, AZ, 1989.
- [4] Yao, C. S., Lin, J. C. and Allan, B. G., "Flow-filed measurement of device-induced embedded streamwise vortex on a flat plate", *1st AIAA Flow Control Conference*, St. Louis, MO, 2002.
- [5] Ashill, P. R., Fulker, J. L. and Hackett, K. C., "Research at DERA on sub boundary layer vortex generators (SBVGs)", *39th Aerospace Science Meeting and Exhibit*, Reno, NV, 2001.
- [6] Jenkins, L., Gorton, S. A. and Anders, S., "Flow control device evaluation for an internal flow with an adverse pressure gradient", *40th AIAA Aerospace Sciences Meeting & Exhibit*, Reno, NV, 2002.
- [7] Allan, B. G., Yao, C. S. and Lin, J. C., "Numerical simulations of vortex generator vanes and jets on a flat plate", *1st AIAA Flow Control Conference*, St. Louis, MO, 2002.
- [8] Torii, K. and Yanagihara, J. I., "The effects of longitudinal vortices on heat transfer of laminar boundary layers", *JSME International Journal Series II*, Vol. 32, No. 3, 1989, pp. 395-402.
- [9] Yanagihara, J. I. and Torii, K., "Enhancement of laminar boundary layer heat transfer by a vortex generator", *JSME International Journal Series II*, Vol. 35, No. 3, 1992, pp. 400-4405.
- [10] Angele, K. P. and Muhammad-Klingmann, B., "The effect of streamwise vortices on the turbulence structure of a separating boundary layer", *European Journal of Mechanics-B/Fluids*, Vol. 24, Issue 5, 2005, pp. 539-554.
- [11] Lin, J. C., Robinson, S. K., McGhee, R. J. and Valarezo, W. O., "Separation control on high-lift airfoils via micro-vortex generators", *Journal of Aircraft*, Vol. 31, No. 6, 1994, pp. 1317-1323.
- [12] Lin, J. C., Selby, G. V. and Howard, F. G., "Exploratory study of vortex-generating devices for turbulent flow separation control", *29th Aerospace Sciences Meeting*, Reno, NV, 1991.
- [13] Godard, G. and Stanislas, M., "Control of a decelerating boundary layer. Part 1: Optimization of passive vortex generators", *Aerospace Science Technology*, Vol. 10, Issue 3, 2006, pp. 181-191.
- [14] Velte, C. M., Hansen, M. O. L. and Cavar, D., "Flow analysis of vortex generators on wing sections by stereoscopic particle image velocimetry measurements", *Environmental Research Letters*, Vol. 3, No. 1, 2008.
- [15] Stillfried, F. V., Wallin, S. and Johansson, A. V., "Evaluation of a vortex generator model in adverse pressure gradient boundary layers", *AIAA Journal*, Vol. 49, No. 5, 2011, pp. 982-993.
- [16] Kerho, M., Hutcherson, S., Blackwelder, R. F. and Liebeck, R. H., "Vortex generators used to control laminar separation bubbles", *Journal of Aircraft*, Vol. 30, No. 3, 1993, pp. 315-319.
- [17] Velte, C. M., Okulov, V. L. and Naumov, I. V., "Regimes of flow past a vortex generator", *Technical Physics Letters*, Vol. 38, Issue 4, 2012, pp. 379-382.
- [18] Yanagihara, J. I. and Torii, K., "Heat transfer augmentation by longitudinal vortices rows", *Experimental heat transfer, Fluid mechanics and Thermodynamics*, 1993, pp. 560-567.
- [19] Narasimha, R. and Prasad, S. N., "Leading edge shape for flat plate boundary layer studies", *Experiments in Fluids*, Vol. 17, Issue 5, 1994, pp. 358-360.
- [20] Kwon, K. J., "Experimental study on aerodynamic and flow field characteristics of elliptic airfoils", *Dissertation*, Korea Advanced Institute of Science and Technology, 2006.
- [21] Prasad, A. K., "Stereoscopic particle image velocimetry", *Experiments in Fluids*, Vol. 29, Issue 2, 2000, pp. 103-116.
- [22] PIVview 3C, PIVTEC, Gottingen, Germany; software available at <http://www.pivtec.com/>

[23] Uncertainty analysis particle image velocimetry. ITTC-Recommended Procedures and Guidelines, 2008.

[24] Assessment of experimental uncertainty with application of wind tunnel testing. AIAA Standard S-071A-1999

[25] Fluent 15.0, ANSYS, Pennsylvania, United States; software available at <http://www.ansys.com>

[26] Menter, F. R., Lantry, R. B., Likki, S. R., Suzenn, Y. B., Huang, P. G. and Volker, S., "A correlation-based transition model using local variables-Part I: Model formulation", *Journal of Turbomachinery*, Vol. 128, Issue 3, 2004, pp. 413-422.

[27] Jiang, M., Machiraju, R. and Thompson, A., *Detection*

and visualization of vortices, Visualization Handbook, Academic Press, 2004.

[28] Strawn, R. C., Kenwright, D. N. and Ahmad, J., "Computer visualization of vortex wake systems", *AIAA Journal*, Vol. 37, No. 4, 1999, pp. 511-512.

[29] Görtz, S., "Realistic simulations of delta wing aerodynamics using novel CFD methods", *Dissertation*, Royal Institute of Technology, 2005.

[30] Lam, K. M. and Wei, C. T., "Numerical simulation of vortex shedding from an inclined flat plate", *Engineering Applications of Computational Fluid Mechanics*, Vol. 4, No. 4, 2010, pp. 569-579.